machines

MDPI

Article

A Comparative Study of Pole–Slot Combination with Fractional Slot Concentrated Winding in Outer Rotor Permanent Magnet Synchronous Generator for Hybrid Drone System

Jeongwon Kim, Ju Lee and Hyunwoo Kim *

Department of Electrical Engineering, Hanyang University, Seoul 04763, Republic of Korea; kjw0427@hanyang.ac.kr (J.K.); julee@hanyang.ac.kr (J.L.)
* Correspondence: khw7481@hanyang.ac.kr

Abstract: This paper is a comparative study of pole–slot combinations with fractional slot concentrated windings in an outer rotor permanent magnet synchronous generator (ORPMSG) for a hybrid drone system. Fractional slot machines have been studied for automotive applications because of their high performance and simple winding manufacturing, compared with those of integer slot machines. In this study, four pole–slot combinations of ORPMSG with fractional slot concentrated windings were selected for comparison with the performance of the hybrid drone system. Based on the results of a finite element analysis (FEA), the machines were analyzed for cogging torque, back electromagnetic force (BEMF), torque, and electromagnetic loss under the same conditions as the machine specifications. Among the four pole–slot combinations of the ORPMSM, a one pole–slot model of the ORPMSG was selected, considering the performances of the machines. The selected pole–slot model of the ORPMSG was manufactured, and experiments were conducted on the manufactured model to verify the FEA results. Finally, the effectiveness of the comparative study of pole–slot combination with fractional slot concentrated winding in ORPMSM was verified by comparing the FEA and experimental results.

Keywords: concentrated winding; fractional slot; hybrid drone system; outer rotor permanent magnet synchronous generator (ORPMSG); pole–slot combination

check for updates

Citation: Kim, J.; Lee, J.; Kim, H. A Comparative Study of Pole–Slot Combination with Fractional Slot Concentrated Winding in Outer Rotor Permanent Magnet Synchronous Generator for Hybrid Drone System. *Machines* **2024**, *12*, 464. https://doi.org/10.3390/machines12070464

Academic Editor: Ahmed Abu-Siada

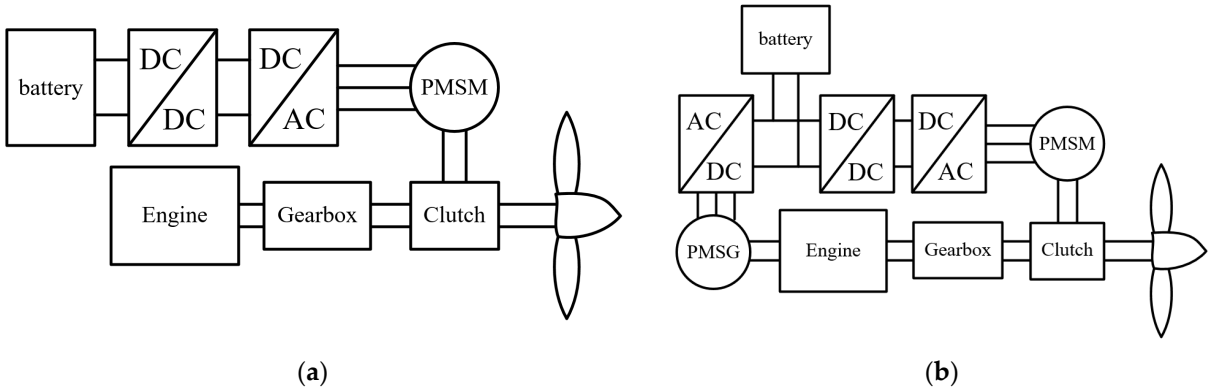
Received: 1 June 2024
Revised: 8 July 2024
Accepted: 8 July 2024
Published: 10 July 2024

Copyright: © 2024 by the authors. Licensee MDPI, Basel, Switzerland. This article is an open access article distributed under the terms and conditions of the Creative Commons Attribution (CC BY) license (https://creativecommons.org/licenses/by/4.0/).

1. Introduction

Recently, with technological developments related to unmanned aerial mobility (UAM), the applications of drones have been rapidly expanding in various fields, including military, logistics transportation, medicine, agriculture fields, and disaster observation [1–6]. The World Economic Forum (WEF) designated it as the representative field that led to the fourth industrial revolution. Drones are a complex industry that combines cutting-edge technologies such as aviation, Information and Communications Technology (ICT), and Sofeware (SW), and they have growth potential in production and operation [7,8]. Accordingly, research on drone technology has received significant attention, both domestically and abroad [9].

Because the flight time of a drone system is limited by its fuel or battery, the most challenging issue in drone systems is the high energy density of the propulsion system [10,11]. Hybrid drone systems have been studied to achieve propulsion systems with high energy densities. Figure 1 shows a hybrid drone system. A conventional hybrid drone system comprises a battery, engine, fuel pack, motor, and drive as shown in Figure 1a [12]. Due to limited fuel and battery, drone systems generally have a flight time of approximately 30 min. If the continuous operation of a drone system is required, it must be fueled or have its battery charged during its flight [13–15]. To address these shortcomings, several studies have addressed increasing energy density and improving flight time. Hybrid engine–generator drone systems have received significant attention in several studies [16–19].



(**a**) (**b**)

Figure 1. Topology of hybrid drone system: (**a**) conventional; (**b**) engine–generator.

Figure 1b shows the hybrid engine–generator system. Compared with a conventional drone system, the hybrid drone system includes the hybrid engine–generator system with a permanent magnet synchronous generator (PMSG). When the drone system is propelled by a motor, the PMSG generates electrical energy from the engine, which charges the battery of the hybrid drone system. Although the overall weight of the hybrid drone system increases as the PMSG is increased, the flight time can increase because the PMSG supplies electrical energy to the battery. Therefore, in the hybrid drone system with the engine–generator, the efficiency of the PMSG is important for improving the flight time [20,21].

Since the drone system operates in the sky, a highly reliable system is required [22,23]. Therefore, a stable power supply is necessary under all conditions. PMSG is required in hybrid drone systems to minimize total harmonic distortion (THD) of the back electromagnetic force (BEMF) and the cogging torque because of the inherent pulsation, vibration, noise, and high-quality electric energy. These issues can be resolved by using a fractional slot concentrate winding (FSCW). FSCWs are excellent at reducing harmonics and have a low cogging torque. Furthermore, they have excellent manufacturability, and high efficiency and high torque density, due to their short end coils [24,25].

Several studies have been conducted to investigate the benefits and limitations of different FSCW machines [26–29]. In [26], the characteristics of pole–slot combination in electrical machine are analyzed based on the Star of slots. Since it does not take into account the spatial harmonics by slot, the nonlinear characteristics by magnetic saturation, and the flux leakage characteristics of the electrical machine, the comparison study according to pole–slot combinations should be conducted using FEA. In [27], a design of an FSCW generator for low cogging torque is studied. In this research, a comparative study of pole–slot combinations of FSCW generators was performed based on the analytical method. However, high-accuracy comparisons were not conducted based on FEA to consider the magnetic saturation and the magnetic flux leakage. In [28] and [29], a comparison study was conducted based on FEA for highly reliable characteristics according to the pole–slot combination of an FSCW permanent magnet synchronous motor. Although there are comparative studies according to the pole–slot combinations, no studies have been conducted comparing the ORPMSG or THD of the BEMF. In this paper, we extend this and perform a comparative analysis of various FSCW pole–slot combinations in ORPMSG. Through this, an excellent pole–slot combination is derived for drone generators, and the reliability of the analysis results is verified through the manufacture and testing of a prototype.

In this paper, the characteristics of pole–slot combinations with fractional slot concentrated winding in an outer rotor permanent magnet synchronous generator (ORPMSG) were investigated for a hybrid drone system. Four pole–slot combinations were selected to compare characteristics such as the BEMF, cogging torque, torque ripple, and efficiency. Under the same PM material, core material, and slot area conditions, the pole–slot combination models were analyzed using finite element analysis (FEA) in ANSYS Maxwell. Based on the

analysis results, the optimal pole–slot combination was selected. Furthermore, the selected pole–slot combination model was manufactured, and an experiment was performed to verify the characteristics of the ORPMSG. Finally, the effectiveness of the comparison with pole–slot combination models was verified.

This paper is organized as follows. In Section 2, the basic principles and equivalent circuit of the ORPMSG are discussed. In Section 3, the characteristics of the pole–slot combination models are discussed using FEA. In Section 4, a comparison between the FEA and prototype experiment is discussed. Finally, the conclusions are presented in Section 5.

2. Principle and Equivalent Circuit of PMSG

The permanent magnet synchronous motor and generator exhibit inverse input and output correlations. When mechanical power causes the rotor of a PMSG to rotate, the magnetic flux from the permanent magnets induces a no-load voltage (back electromotive force, BEMF) in the armature coil. When a load is connected to the stator, an electric current passes through the winding and a voltage is induced due to the armature reaction [30,31]. The voltage induced by the armature reaction is expressed as follows:

$$e_a = -\frac{d\lambda_a}{dt} = -L_a \frac{di_a}{dt} \tag{1}$$

where e_a is induced voltage by the armature reaction, λ_a is the armature reaction flux linkage, L_a is the phase inductance, and i_a is the phase current. Equation (1) can be expressed in the frequency domain as follows:

$$E_a = jX_a I_a \tag{2}$$

where X_a is the armature reaction reactance. If a leakage flux exists in the PMSG, the induced voltage by leakage flux linkage can be expressed as follows:

$$E_l = jX_l I_a \tag{3}$$

where X_l is the leakage reactance. Considering the phase resistance, armature reaction reactance, and leakage reactance, the equivalent circuit for a single phase of the PMSG is shown in Figure 2. From Figure 2, the voltage equation of the PMSG is expressed as follows:

$$V = E_0 - R_a I_a - jX_s I_a \tag{4}$$

where V is the output voltage, E_0 is the BEMF, R_a is the phase resistance of the armature, and X_s is the synchronous reactance which is the sum of the armature and leakage reactances. The output voltage of the PMSG is obtained by subtracting the voltage drops in the synchronous reactance and resistance from the BEMF. If the PMSG rotates with mechanical power and the load is connected to the PMSG, a magnetic torque is generated in the direction opposite to the rotational direction of the mechanical power. Therefore, mechanical power is required to overcome the torque in PMSG. Equation (5) expresses the output power based on the energy conversion.

$$P_e = T_G \omega_s - P_{loss} = V I_a \cos\theta \tag{5}$$

where P_e is the output power, T_G is the mechanical torque by the engine, ω_s is the rotational speed, P_{loss} is the loss of the PMSG, and θ is the angle of the power factor. From Equation (5), the required torque of the PMSG can be expressed as follows:

$$T_G = \frac{V I_a \cos\theta + P_{loss}}{\omega_s} \tag{6}$$

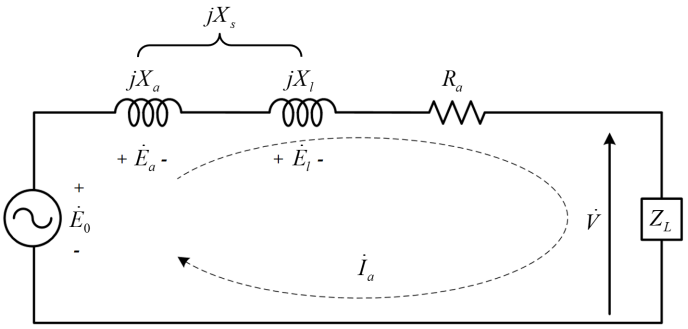


Figure 2. Equivalent circuit of PMSGs.

From Equation (6), the torque is determined by the output voltage. Furthermore, because the output voltage is determined by the BEMF, the harmonic component of the BEMF is an important component of the PMSG. In a hybrid drone system, the PMSG is derived from engine and battery charging. Therefore, the PMSG has a low cogging torque and total harmonic distortion (THD) of the BEMF for reliable or hybrid drone systems. In this paper, the cogging torque and THD of the BEMF in the PMSG are analyzed according to a pole–slot combination based on FEA as in Section 3.

3. Comparison of ORPMSG Models

3.1. Constraints of Comparison Models

Analytical models are used to compare the features of the pole–slot combinations under identical conditions, taking into account the constraints. Table 1 shows the constraints on the analysis models. The characteristics of the pole–slot combinations are analyzed under the same conditions of motor size, total slot area, total volume of the PM, slot opening, and pole arc ratio. The generator used in this paper requires an output of more than 1 kW at 2000 rpm. Since the generator charges a battery of 48 V_{dc} at 5000 rpm, the line to line voltage of the generator at 5000 rpm is greater than 57 V. In Section 3.2, the pole–slot combination models under the conditions as shown in Table 1 are discussed. The rotor and stator core in this paper use lamination electrical steel such as 50PN470 in POSCO which is widely used in the industry [32,33].

Table 1. Constraints of ORPMSG for comparing pole–slot combination models.

Content	Value	Unit
Rated speed	2000	rpm
Rated power	1	kW
Battery voltage @ 5000 rpm	48	V_{dc}
Required voltage @ 5000 rpm	57	V
Rotor outer/inner diameter	148.8/128	mm
Stator outer/inner diameter	127/76.24	mm
Length of airgap	0.5	mm
Stack length	15	mm
Pole arc ratio	0.8	-
Total volume of PM	1671	mm^3
Slot opening	6	mm
Total slot area	1917	mm^2
Slot fill factor	40	%
Material of PM	N40UH	-
Material of rotor and stator core	50PN470	-

3.2. Comparison Models of Pole–Slot Combinations for ORPMSG

The generator in the hybrid drone system requires a low cogging torque and total harmonic distortion (THD) of the BEMF. In PMSG, the cogging torque and THD of the

BEMF are determined by the pole–slot combination [34]. When the pole–slot combination is selected, we consider the following:

- The larger the winding coefficient, the higher the BEMF and torque generated.
- The least common multiple (LCM) of the poles and slots is proportional to the cogging torque frequency. In general, the frequency of the cogging torque can increase, and the magnitude of the cogging torque can reduce as the LCM increases.
- Fractional slot machines contain fewer harmonics than do integer slot machines [34].
- The motor periodicity is defined as the greatest common divisor (GCD) of the pole pairs and slots. The symmetry of the magnetic flux density is determined by the GCD, which is the motor periodicity [35,36].

Considering the characteristics of pole–slot combination, we select four pole–slot combinations: 10P12S(M1), 14P12S(M2), 14P18S(M3), and 16P18S(M4). Table 2 shows a comparison of selected pole–slot combinations, and Figure 3 shows the structures of the selected pole–slot combinations. In Section 4, the characteristics of the pole–slot combinations under the conditions shown in Table 1 are compared.

Table 2. Comparison of selected pole–slot combinations.

Content	M1	M2	M3	M4
Pole/slot	10P12S	14P12S	14P18S	16P18S
LCM of poles and slots	60	84	126	144
GCD of pole pairs and slots	1	1	1	2
Winding factor	0.933	0.933	0.902	0.945
Number of serial turns per phase	104	88	96	84

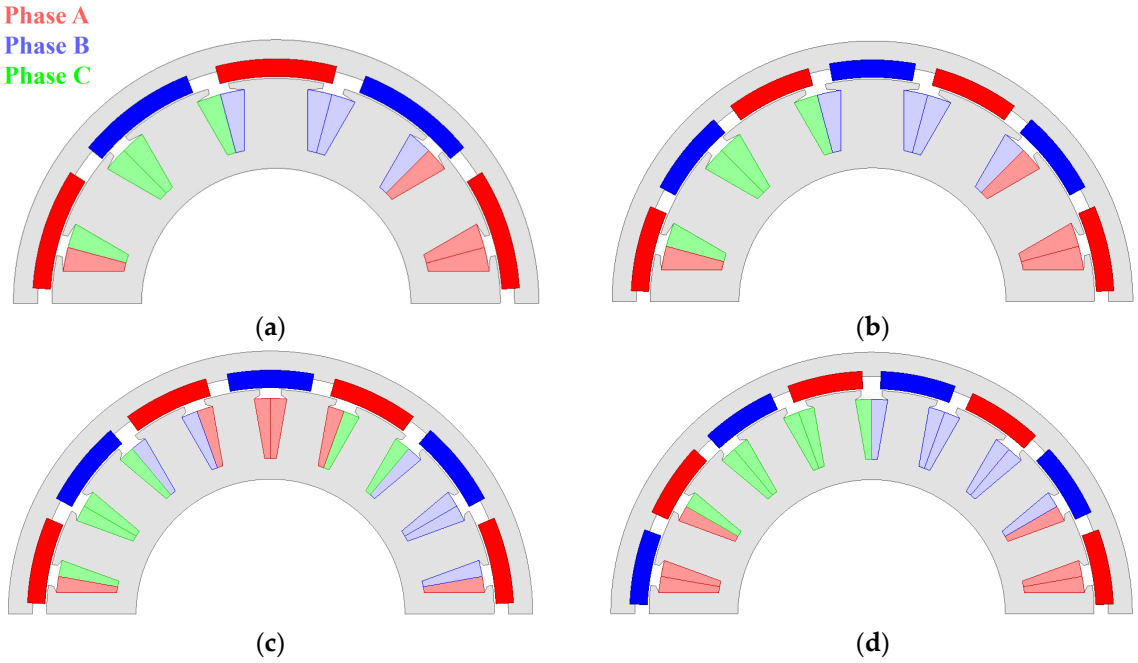


Figure 3. Structure of selected pole–slots combinations: (**a**) 10P12S (M1); (**b**) 14P12S (M2); (**c**) 14P18S (M3); (**d**) 16P18S (M4).

4. Comparison of the Characteristics of the Pole–Slot Combination

In Section 3, the electromagnetic characteristics of the four selected pole–slot combinations are compared using FEA in ANSYS Maxwell 2021R1. In Section 4.1, open circuit characteristics including the cogging torque and THD of BEMF are analyzed. In Section 4.2, the load characteristics are compared when a sinusoidal current is applied to the ORPMSG,

and an external circuit analysis is performed to compare the generator characteristics according to the resistance load.

4.1. No-Load Characteristic

4.1.1. Airgap Magnetic Flux Density

The harmonic components of the magnetic flux density in the airgap are related to the flux linkage and can have significant negative effects on the harmonics of the BEMF, power, vibration, and noise. Figure 4 shows the distribution of the magnetic flux density according to the pole–slot combination. Figure 4 shows that each model is designed so that the teeth and yoke are saturated at 1.5 to 2.2 T considering the magnetic saturation. Figure 5 shows the airgap magnetic flux density based on the pole–slot combinations. As the number of poles increases, the waveform of the airgap magnetic flux density becomes more sinusoidal due to the increased leakage magnetic flux density. Furthermore, the magnitude of the airgap magnetic flux density decreases with the slot opening as the magnetic reluctance increases. Figure 6 shows the fast Fourier transformation (FFT) results of the airgap magnetic flux density according to the pole–slot combinations. From Figure 6, the fundamental frequency is decided by the number of pole pairs. Since the pole–slot combinations are fractional slots with a concentrated winding, there is a subharmonic component whose frequency is lower than the fundamental frequency. The subharmonic component of M2 is higher than those of the other models. Excluding the fundamental harmonic and subharmonic components, the harmonic components are caused by the permanent magnet and slot. Because the pole arc ratio and slot opening are the same, the harmonic components of the permanent magnet and slot are similar.

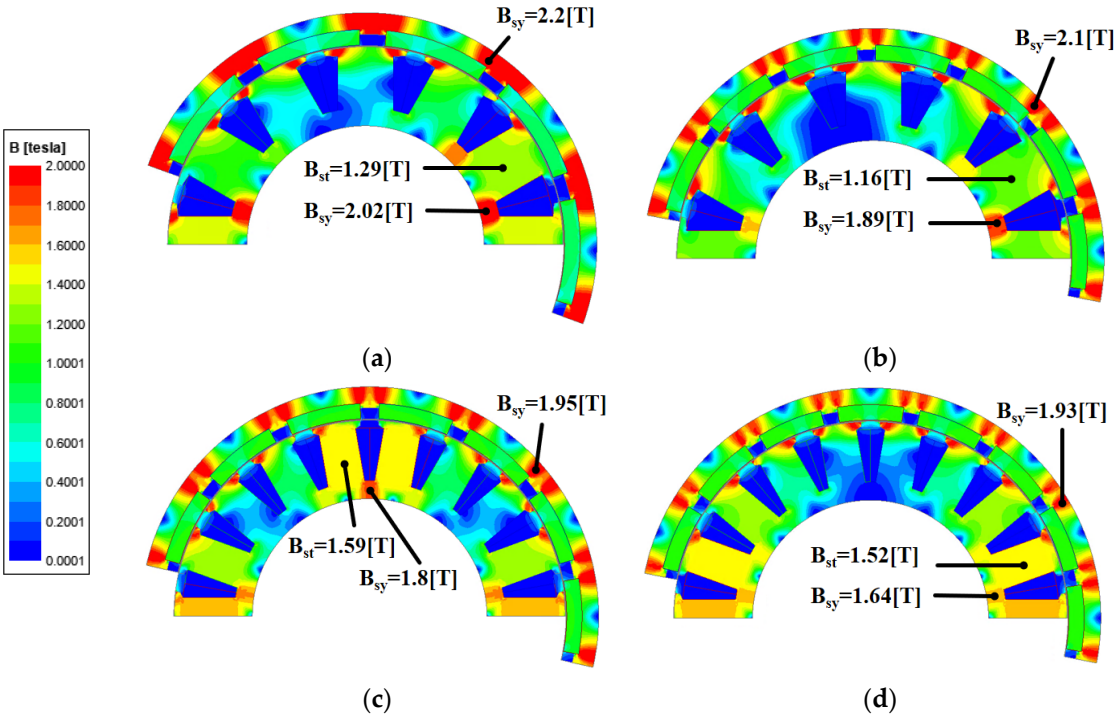


Figure 4. Magnetic flux density distribution of analysis models: (**a**) M1; (**b**) M2; (**c**) M3; (**d**) M4.

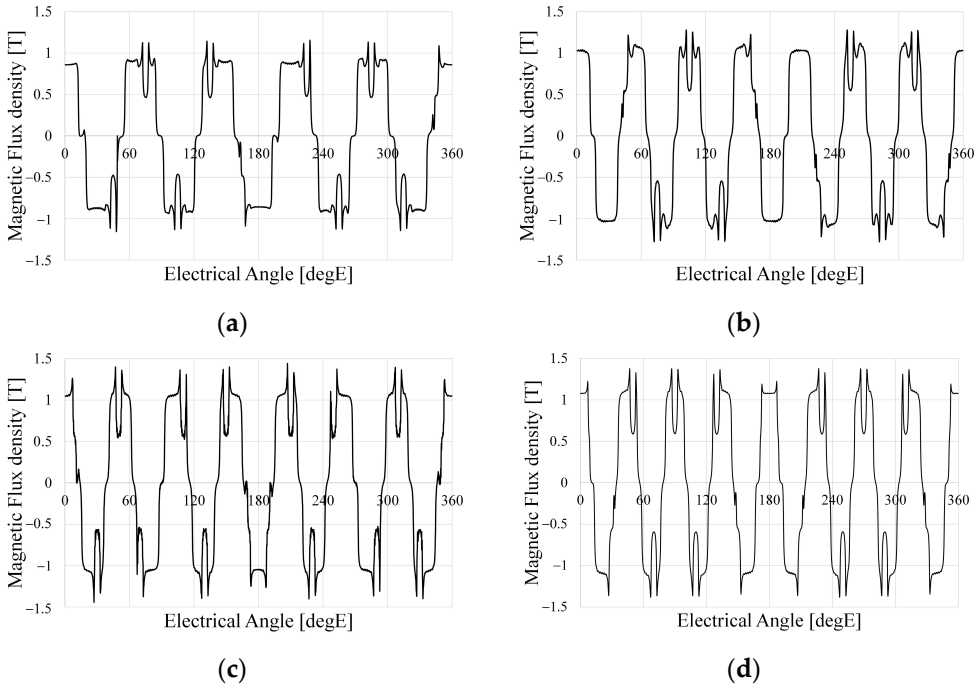


Figure 5. Airgap magnetic flux density of analysis models: (**a**) M1; (**b**) M2; (**c**) M3; (**d**) M4.

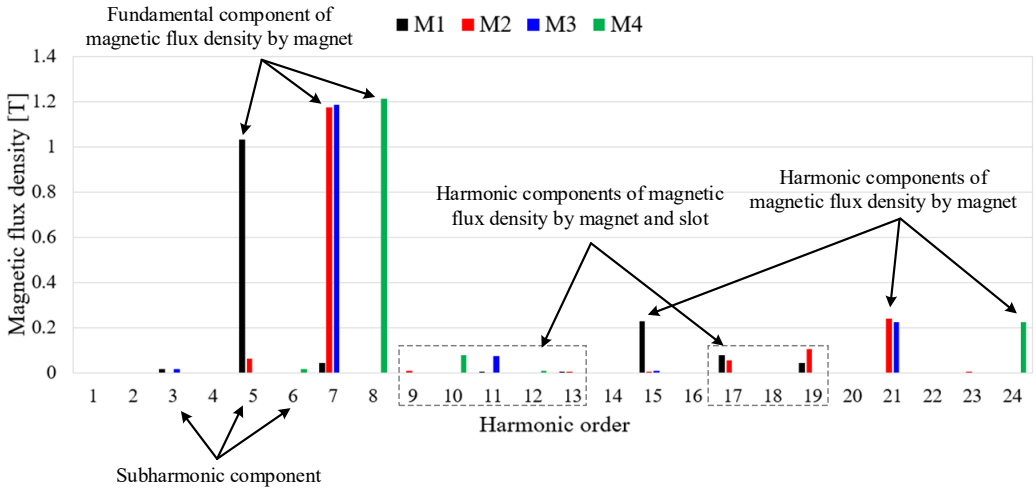


Figure 6. FFT results of the airgap magnetic flux density according to the pole–slot models.

4.1.2. Cogging Torque

The cogging torque is the reluctance torque that aligns the magnetic flux of the permanent magnet and the tooth structure, and it is expressed as follows [37]:

$$T_{cog}(\alpha) = \frac{\pi L_{stk}}{4\mu_0}\left(R_2^2 - R_1^2\right)\sum_{n=1}^{\infty} nN_L G_{nN_L} B_{nN_L} \sin(nN_L\alpha) \quad (7)$$

where μ_0 is the permeability in the air, N_L is $LCM(N_s,N_p)$, N_p and N_s are the number of poles and number of slots, respectively, R_1, R_2, and L_{stk} are the inner and outer diameters of the air gap and the stack length, respectively, α is the rotor position, and G_{nNL} and B_{nNL} are the Fourier coefficients of the airgap relative permeance and airgap flux density, respectively. From Equation (7), the period of the cogging torque is determined by the LCM of the pole and the slot number, and the cogging torque can be reduced as the period of the cogging torque is reduced. Since the mechanical frequency of the cogging torque is equal

to the LCM of the numbers of poles and slots, the electrical period of the cogging torque is expressed as follows:

$$t_{cogging} = \frac{360}{LCM(N_s, N_p)} \frac{N_p}{2} \text{ [degE]} \quad (8)$$

Table 3 shows the cogging torque characteristics of the pole–slot combination models. From Equation (8), the electrical period of the cogging torques of M1, M2, M3, and M4 are calculated as 30 degE, 30 degE, 20 degE, and 20 degE, respectively. Therefore, the fundamental harmonic orders of cogging torque of M1, M2, M3, and M4 are 12, 12, 18, and 18, respectively. The cogging torques of M3 and M4 are lower than those of M1 and M2 because the periods of the cogging torques are higher. Figure 7 shows the cogging torque waveform and FFT result of pole–slot combination models. The cogging torque of M3 is better than that of other models. The fundamental order of the cogging torque of M3 is 18 and the fundamental component of the cogging torque is near zero as shown in Figure 7b. The pole arc ratio and slot opening are affected by the cogging torque [38]. The cogging torque of M3 is optimized under the conditions of the slot opening and pole arc ratio as shown in Table 1. Since the slot opening and pole arc ratio are selected as constraints, the fundamental component of M3 is near zero. Consequently, the cogging torque of M3 is better than that of the other models.

Table 3. Comparison of the cogging torque of the analysis models.

Content	M1	M2	M3	M4	Unit
Electrical period	30	30	20	20	degE
Fundamental harmonic order	12	12	18	18	-

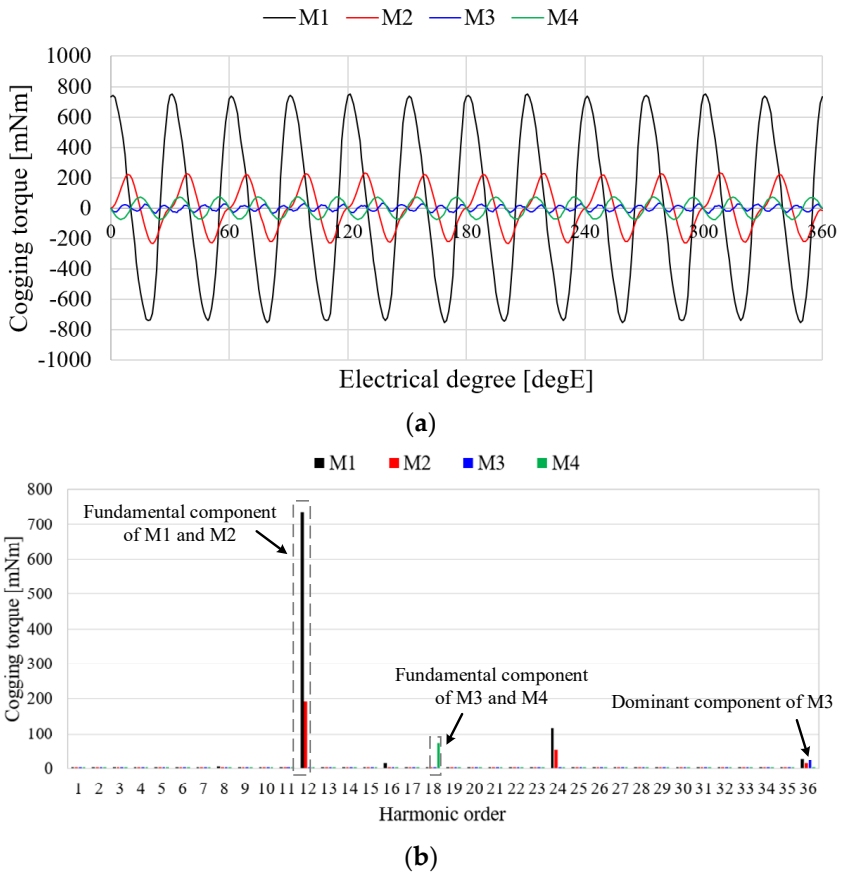


Figure 7. Cogging torques of the analysis models: (**a**) Waveform; (**b**) FFT result.

4.1.3. Line to Line Voltage

From Equation (5), the harmonic component of the BEMF is an important performance factor because the torque ripple is determined by the voltage. Furthermore, the harmonic component of the BEMF is also important since the generator charges the battery. To compare the harmonic components of the pole–slot combinations, the THD of the BEMF is defined as follows:

$$THD = \frac{\sqrt{\sum_{h=2,3,\cdots}^{\infty} V_h^2}}{V_1} = \frac{\sqrt{V^2 - V_1^2}}{V_1} \quad (9)$$

where V_1 is the fundamental component of the voltage, V_h is the nth harmonic component, and V is rms value of the voltage. From Equation (9), THD of the BEMF is the number of harmonics in the fundamental waveform. This implies that a large THD of the BEMF includes a high harmonics component of the voltage. Therefore, when designing a generator for charging the battery in the drone system, the pole–slot combination is an important design method by which to minimize the THD of the BEMF. Figure 8a shows the waveform of the line to line voltage and Figure 8b shows the FFT result of the line to line voltage. As shown in Figure 8a, the waveforms of M3 and M4 are more sinusoidal than are those of M1 and M2. The harmonic components of M3 and M4 are lower than are those of M1 and M2 as shown in Figure 8b. Table 4 shows the voltage characteristics of the analysis models. The line to line voltage of M3 is higher than those of the other models, and THD of M3 is lower than those of the other models as shown in Table 4.

Table 4. Voltage characteristics of the analysis models.

Content	M1	M2	M3	M4	Unit
Phase voltage (fundamental)	48.2	48.9	51	48.5	V_{max}
Line to line voltage (fundamental)	83.4	84.8	88.4	84	V_{max}
Phase voltage THD	5.36	9.17	2.21	5.75	%
Line to line voltage THD	2.22	4.71	0.36	0.52	%

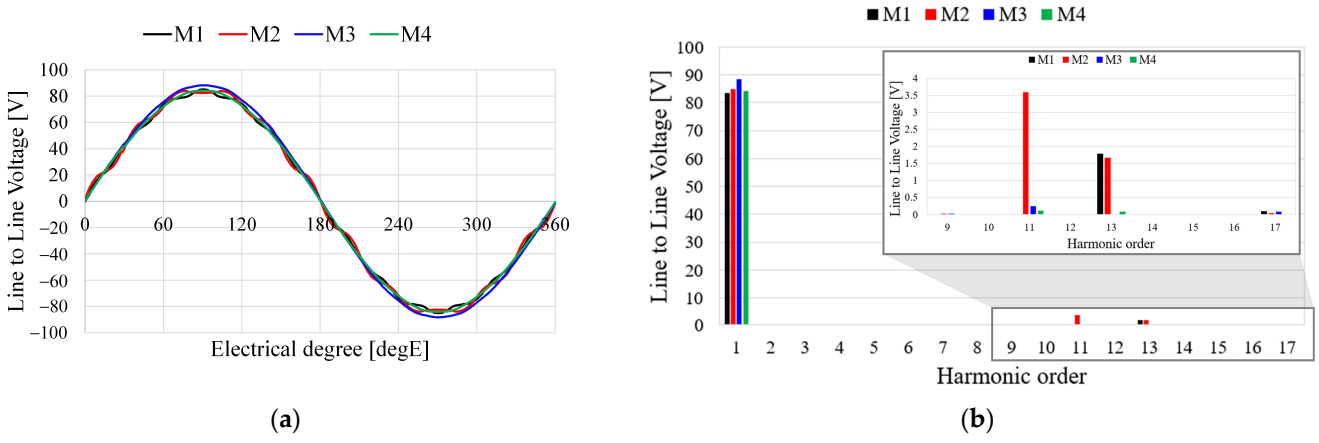


Figure 8. Line to line voltages of the analysis models: (**a**) Waveform; (**b**) FFT results.

4.2. On-Load Characteristic

4.2.1. Torque Characteristics by Sinusoidal Current

Because the torque ripple is related to the vibration and noise of the generator, it is an important characteristic that must be considered when designing a generator. The load characteristics are analyzed and compared with pole–slot combinations when an ideal

sinusoidal current source is applied to the generator. In general, when a sinusoidal current is applied to a generator, its torque can be expressed as:

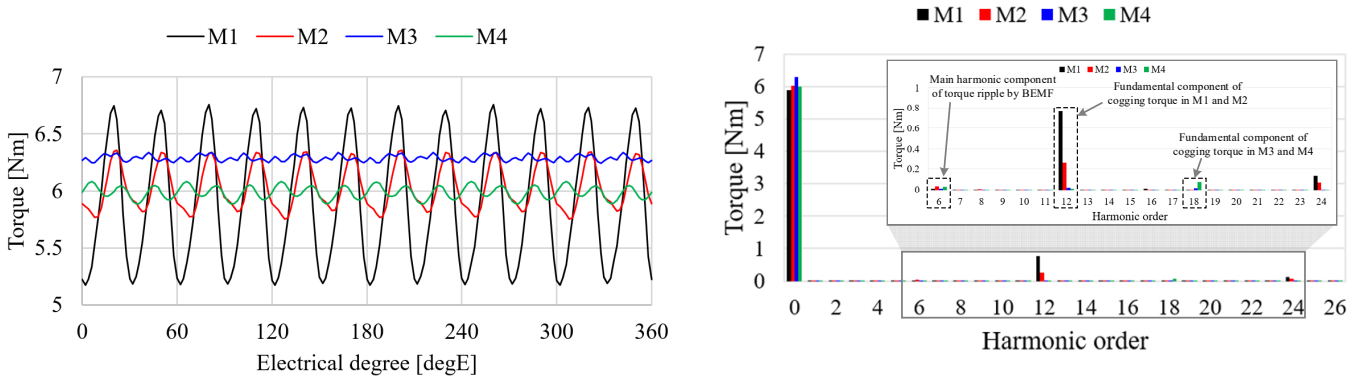
$$T_e = \frac{e_a i_a + e_b i_b + e_c i_c}{\omega_m} = \frac{3}{2}\frac{E_1 I_m}{\omega_m} + \sum_{n=6k} \frac{3}{2}\frac{-E_{n-1} + E_{n+1}}{\omega_m} I_m \cos(n\omega t + \varphi_n) \quad (10)$$

where T_e is the torque of the generator, e_a, e_b, and e_c are each a phase BEMF of the generator, respectively, i_a, i_b, and i_c are each a phase current of the generator, ω_m is the rotational speed, E_1 is the magnitude of the fundamental component of the BEMF, I_m is the magnitude of the current, E_{n-1} and E_{n+1} are the $(n-1)$th and $(n+1)$th harmonic components of the BEMF, respectively, n is the harmonic order, and φ_n is the phase angle of the torque.

From Equation (10), the torque ripple is determined from the harmonic component of the BEMF. Because M3 and M4 are more sinusoidal than are M1 and M2 as shown in Figure 9, the torque ripples of M3 and M4 are lower than are M1 and M2. Figure 9 shows the torque characteristics of each model. Figure 9a shows the torque waveform of the torque. The average torque of M3 is higher than those of the other models, and the torque ripple of M3 is lower than those of the other models. Figure 9b shows the FFT results of the torque as shown in Figure 9a. As shown in Equations (7) and (10), the torque ripple has the harmonic component owing to the cogging torque and harmonics of the BEMF. In a fractional slot with a concentrated winding, the main torque ripple is determined by the cogging torque because the harmonic of the BEMF is lower. Table 5 shows the comparison with torque characteristics of each analysis model. The average torque of M3 is 6.25%, 4.31%, and 5% higher than those of M1, M2, and M4, respectively, and the torque ripples of M3 are 25.2%p, 8.6%p, and 1.8%p lower than those of M1, M2, and M4, respectively. Consequently, when the sinusoidal current source is applied to the generator, the torque characteristics of M3 are superior to those of the other models.

Table 5. Torque characteristics by sinusoidal current.

Content	M1	M2	M3	M4	Unit
Rated current			30		A_{rms}
Torque	5.92	6.03	6.29	5.99	Nm
Torque ripple	26.7	10.13	1.53	3.29	%



(**a**) (**b**)

Figure 9. Torque of analysis models when the sinusoidal current at 30 A_{rms}: (**a**) Waveform; (**b**) FFT results.

4.2.2. Generator Characteristic for External Resistance Load

To compare the generator characteristics, the external load is accounted for by the resistance load as shown in Figure 10. When BEMF is generated by a mechanical input, the current flowing through the generator is determined by R_a and R_{load}. Figure 11 shows the comparison results of the generator characteristics for an external load when the generator

speed is 2000 rpm. As shown in Figure 11a, because the output current is inversely proportional to the resistance, the output power of the generator increases as the resistance load decreases. The output power for the resistance load of M3 is higher than those of the other models because the BEMF of M3 is higher than those of the other models as shown in Figure 8a. Figure 11b shows the torque ripple of the generator under an external resistance load. The torque ripple of the generator for the external resistance load is determined by the cogging torque and THD of the BEMF as shown in Equations (6) and (9), respectively. As the cogging torque and THD of the BEMF of M3 are lower than those of the other models, the torque ripple of M3 is lower than those of the other models. Figure 11c–e show the PM eddy current loss, core loss, and copper loss, respectively. Since the PM eddy current loss and core loss are determined by the electrical frequency, they increase with the number of poles. Furthermore, as the end turn length decreases and the number of slots increases, the armature resistance decreases. Moreover, the copper loss of M4 is lower than those of the other models. As shown in Figure 11c–e, the main loss of the generator is the copper loss. Figure 11f shows the efficiency of the resistance load in the analysis models. The efficiency of M4 is higher than those of the other models because the copper loss of M4 is lower than those of the other models. Considering the torque ripple and efficiency of the generator, the pole–slot combination is selected as M3(14P18S).

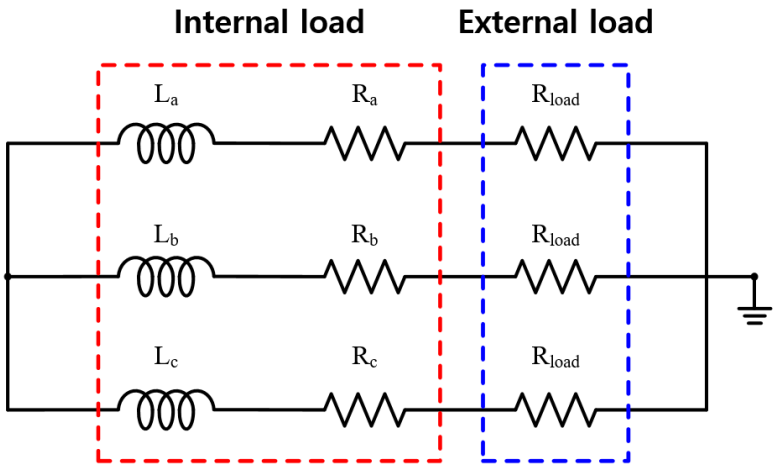
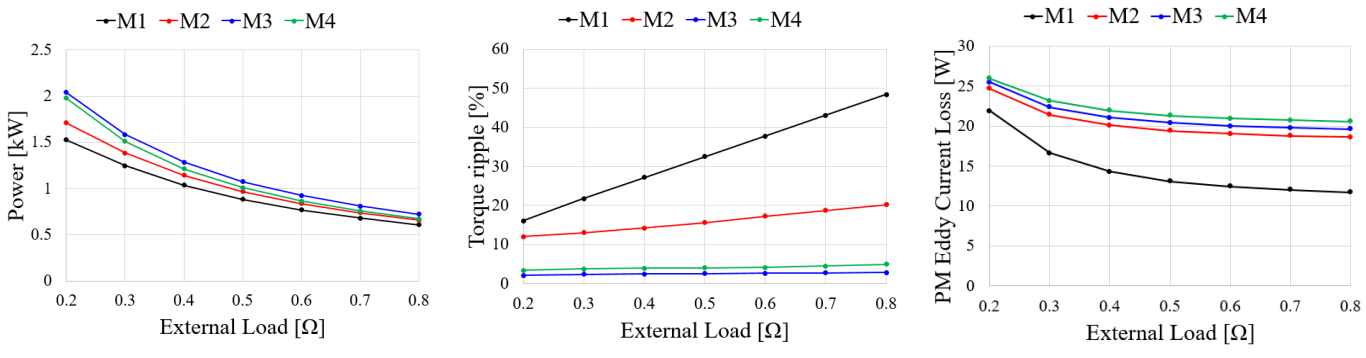


Figure 10. External circuit for analysis of PMSG.



(**a**) (**b**) (**c**)

Figure 11. *Cont.*

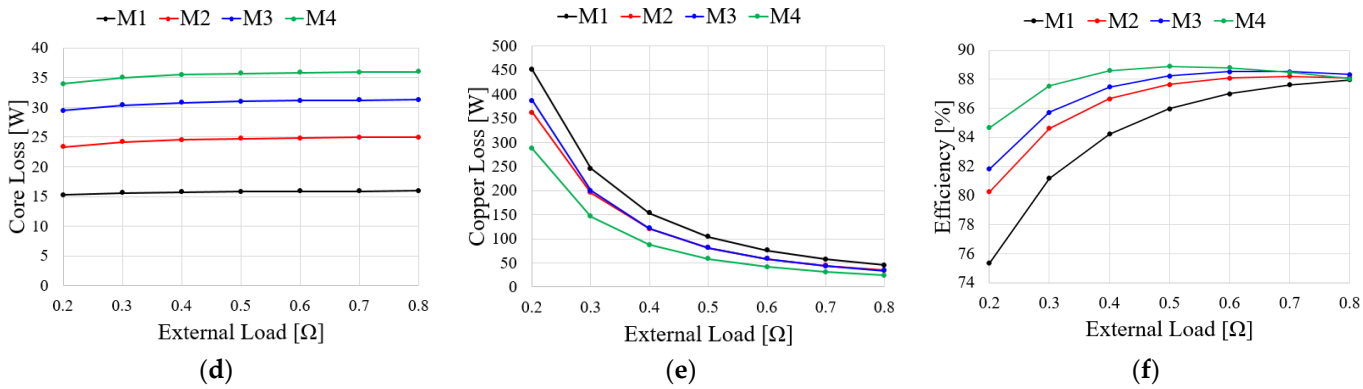


Figure 11. Generator characteristics for the resistance load: (**a**) Power; (**b**) Torque ripple; (**c**) PM eddy current loss; (**d**) Core loss; (**e**) Copper loss; (**f**) Efficiency.

5. Manufacture and Experiment Verification

5.1. Manufacture of Prototype and Experiment Environment

To verify the characteristics of the pole–slot combination, a prototype with a pole–slot combination of 14 poles and 18 slots is manufactured. Figure 12 shows the structure of the prototype. The stator and rotor core are laminated, and the magnetization of the permanent magnet is parallel direction. Figure 13a shows the stator, Figure 13b shows the stator with winding, Figure 13c shows the rotor, and Figure 13d shows the assembled generator. Figure 14 shows the experimental environment. The mechanical input power of the generator is received by the dynamometer, and the electrical output of the generator provides the load through the rectifier. In the power analyzer, the electrical power, efficiency, voltage, and current are analyzed, and the voltage and current waveforms are measured using an oscilloscope and monitoring system.

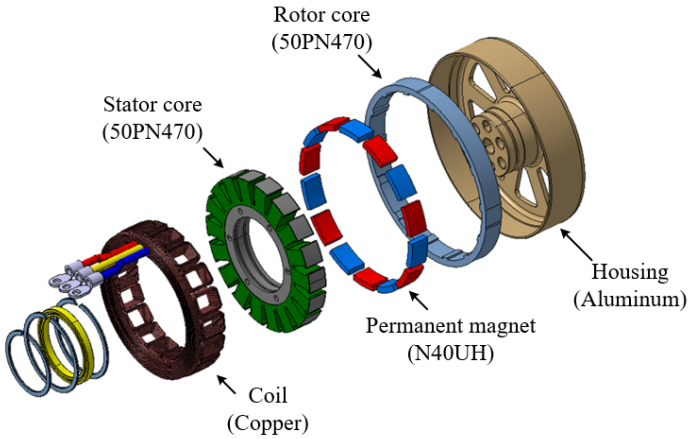


Figure 12. Structure of prototype model.

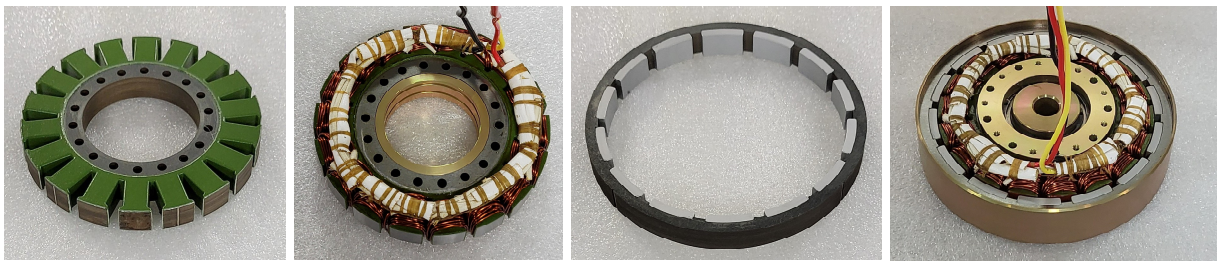


Figure 13. Manufactured prototype: (**a**) Stator; (**b**) Stator with coil; (**c**) Rotor; (**d**) Assembled generator.

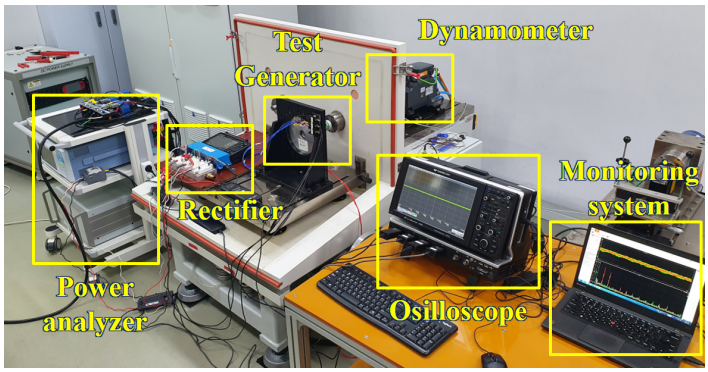


Figure 14. Experimental Environment.

5.2. Performance Verification Comparison of FEA and Experimental Results

Figure 15 shows the characteristics of the no-load test and analysis results according to the speed of the generator. For the no-load test, the induced voltage is the same when comparing with FEA and experimental results. To verify the load characteristics of the generator, a rectifier is considered in the test as shown in Figure 14. The test and analysis results show the input torque, line-to-line voltage, mechanical input, electrical output, and generator efficiency for the same phase current flows. The results in Figure 16a–d show similar trends. In the case of the efficiency and the input power, it was confirmed that the error increased as the speed increased, which is believed to have been caused by an increase in the wind loss due to an increase in speed and an increase in iron loss due to an increase in voltage. The values for each speed item are shown in Table 6. When comprehensively examining the no-load and load characteristics, the FEA analysis results were judged to be sufficiently reliable.

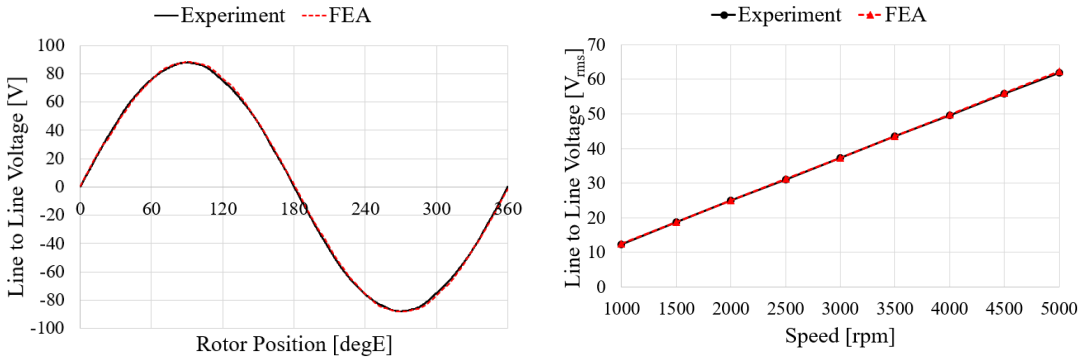


Figure 15. Comparison of FEA and experimental results of the no-load test: (**a**) Waveform at 5000 rpm; (**b**) Line to line voltage.

Table 6. Comparison with FEA and experimental results for load test.

Content	Speed (rpm)	Current (A_{rms})	Torque (Nm)	Output Voltage (V)	Input Power (kW)	Output Power (kW)	Efficiency (%)
Experiment	2000	27.4	5.5	21.8	1.16	0.90	86.32
	3000	17.2	3.8	34.9	1.19	0.95	84.7
	4000	12.7	3.1	47.5	1.28	0.97	78.52
	5000	10	2.6	60.1	1.38	0.98	72.88
FEA	2000	27.4	5.63	22.7	1.19	1.02	86.09
	3000	17.5	3.79	36.1	1.2	1.01	84.51
	4000	12.7	3.06	49.0	1.31	1.03	78.21
	5000	9.99	2.64	61.7	1.43	1.03	72.09

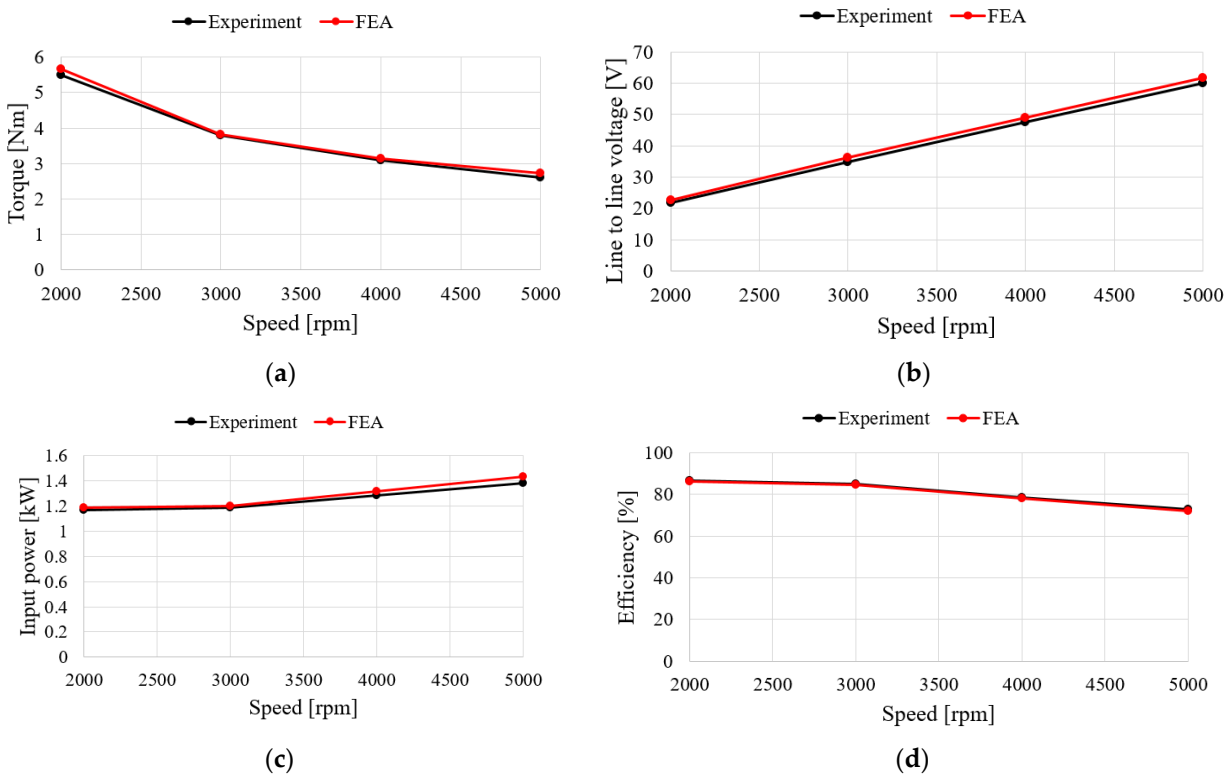


Figure 16. Comparison of FEA and experimental results for load test: (**a**) Torque; (**b**) Line to line voltage; (**c**) Mechanical power; (**d**) Efficiency.

6. Conclusions

In this paper, a harmonic reduction design method was implemented for a hybrid external electric generator for drones. The generator no-load and load characteristics were compared for the following pole and slot combinations: 10P12S(M1), 14P12S(M2), 14P18S(M3), and 16P18S(M4). Each model was selected in fractional slots with a concentrated winding. A comparative analysis was conducted using ANSYS Maxwell 2D FEA. Among the four combinations, 14P18S(M3) exhibited the best performances such as the cogging torque and line-to-line THD characteristics at no load. Additionally, the torque ripple, air gap flux density, and loss characteristics were analyzed during the load. The output and efficiency characteristics of M3 and M4 were excellent. Among these, M4 performed slightly better than M3. However, M3 was superior in terms of the cogging torque and torque ripple. Therefore, to ensure the stability of the drone generator system, M3, which has excellent THD and cogging torque characteristics among the fractional slot models, was proposed. The M3 model has a phase voltage THD that is approximately 3.5 to 7% lower than those of the other models, and its cogging torque and torque ripple are approximately 53% lower than those of the other models.

Author Contributions: Conceptualization, J.K.; methodology, J.K.; software, J.L.; validation, J.K. and H.K.; formal analysis, J.K.; investigation, J.K. and H.K.; resources, J.L.; data curation, J.K.; writing—original draft preparation, J.K.; writing—review and editing, H.K.; visualization, J.K. and H.K.; supervision, H.K.; project administration, J.L.; funding acquisition, J.L. All authors have read and agreed to the published version of the manuscript.

Funding: This research was supported by Korea Electric Power Corporation. (Grant number: R22XO02-02) and in part by the Korea Institute of Energy Technology Evaluation and Planning(KETEP) grant funded by the Korea government(MOTIE) (No. RS-2023-00237024, Development and demonstration of medium-sized variable speed high-power motor).

Data Availability Statement: The data presented in this study are available in this article.

Conflicts of Interest: The authors declare no conflicts of interest.

References

1. Benarbia, T.; Kyamakya, K. A Literature Review of Drone-Based Package Delivery Logistics Systems and Their Implementation Feasibility. *Sustainability* **2022**, *14*, 360. [CrossRef]
2. Rosser, J.C., Jr.; Vignesh, V.; Terwilliger, B.A.; Parker, B.C. Surgical and Medical Applications of Drones: A Comprehensive Review. *JSLS* **2018**, *22*, e2018.00018. [CrossRef]
3. de Jong, S.M. Grand Challenges in Earth Observation Using Unpiloted Airborne Systems. *Front. Remote Sens.* **2020**, *1*, 601737. [CrossRef]
4. ITF. *Ready for Take Off? Integrating Drones into the Transport System*; ITF Research Reports; OECD Publishing: Paris, France, 2021.
5. Shahmoradi, J.; Talebi, E.; Roghanchi, P.; Hassanalian, M. A Comprehensive Review of Applications of Drone Technology in the Mining Industry. *Drones* **2020**, *4*, 34. [CrossRef]
6. Emimi, M.; Khaleel, M.; Alkrash, A. The Current Opportunities and Challenges in Drone Technology. *Int. J. Electr. Eng. Sustain.* **2023**, *1*, 74–89.
7. González-Jorge, H.; Martínez-Sánchez, J.; Bueno, M.; Arias, A.P. Unmanned Aerial Systems for Civil Applications: A Review. *Drones* **2017**, *1*, 2. [CrossRef]
8. Vergouw, B.; Nagel, H.; Bondt, G.; Custers, B. Drone Technology: Types, Payloads, Applications, Frequency Spectrum Issues and Future Developments. *Inf. Technol. Law Ser.* **2016**, *27*, 21–45.
9. Alwateer, M.; Loke, S.W. Emerging Drone Services: Challenges and Societal Issues. *IEEE Technol. Soc. Mag.* **2020**, *39*, 47–51. [CrossRef]
10. Yang, X.; Pei, X. 15-Hybrid system for powering unmanned aerial vehicles: Demonstration and study cases. In *Hybrid Energy System*; Academic Press: Cambridge, MA, USA, 2022; pp. 439–473.
11. Viswanathan, V.; Epstein, A.H.; Chiang, Y.M.; Takeuchi, E.; Bradley, M.; Langford, J.; Winter, M. The challenges and opportunities of battery-powered flight. *Nature* **2022**, *601*, 519–525. [CrossRef]
12. Dannier, A.; Del Pizzo, A.; Di Noia, L.P.; Spina, I. Sizing Procedure of PMSMs for Hybrid Parallel Aircraft Propulsion. In Proceedings of the 2018 IEEE International Conference on Electrical Systems for Aircraft, Railway, Ship Propulsion and Road Vehicles & International Transportation Electrification Conference (ESARS-ITEC), Nottingham, UK, 7–9 November 2018.
13. Jeong, K.S.; Lee, W.Y.; Kim, C.S. Energy management strategies of a fuel cell/battery hybrid system using fuzzy logics. *J. Power Sources* **2005**, *145*, 319–326. [CrossRef]
14. Goh, C.S.; Kuan, J.R.; Danner, A. A fully solar-powered quadcopter able to achieve controlled flight out of the ground effect. *Photovoltaics* **2019**, *27*, 869–878. [CrossRef]
15. Boukoberine, M.N.; Donateo, T.; Benbouzid, M. Optimized Energy Management Strategy for Hybrid Fuel Cell Powered Drones in Persistent Missions Using Real Flight Test Data. *IEEE Trans. Energy Convers.* **2022**, *37*, 2080–2091. [CrossRef]
16. Park, J.H.; Lyu, H.G.; Lee, H.T. Power System Optimization for Electric Hybrid Unmanned Drone. *J. Korean Soc. Aeronaut. Space Sci.* **2019**, *47*, 300–308.
17. Reyner, C.; Hartono, F. The development and testing of 2.4 kW lightweight hybrid power generator unit for multirotor. *AIP Conf. Proc.* **2023**, *2941*, 020045.
18. Xiao, C.; Wang, B.; Wang, C.; Yan, Y. Design of a novel fully-active PEMFC-Lithium battery hybrid power system based on two automatic ON/OFF switches for unmanned aerial vehicle applications. *Energy Convers. Manag.* **2023**, *292*, 117417. [CrossRef]
19. Nurrohaman, M.F.; Titalim, B.A.; Utama, T.H.; Adiprawita, W. Design and Implementation of On-board Hybrid Generator for Rotary Wing Drone. In Proceedings of the 2019 International Conference on Electrical Engineering and Informatics (ICEEI), Bandung, Indonesia, 9–10 July 2019.
20. Li, S.; Gu, C.; Zhao, P.; Cheng, S. A novel hybrid propulsion system configuration and power distribution strategy for light electric aircraft. *Energy Convers. Manag.* **2021**, *238*, 114171. [CrossRef]
21. Zhang, X.; Bowman, C.L.; O'Connell, T.C.; Haran, K.S. Large electric machines for aircraft electric propulsion. *IET Electr. Power Appl.* **2019**, *12*, 767–779. [CrossRef]
22. Boukoberine, M.N.; Zhou, Z.; Benbouzid, M. A critical review on unmanned aerial vehicles power supply and energy management: Solutions, strategies, and prospects. *Appl. Energy* **2019**, *255*, 113823. [CrossRef]
23. Nøland, J.K.; Leandro, M.; Suul, J.A.; Molinas, M. High-Power Machines and Starter-Generator Topologies for More Electric Aircraft: A Technology Outlook. *IEEE Access* **2020**, *8*, 130104–130123. [CrossRef]
24. Reddy, P.B.; El-Refaie, A.M.; Huh, K.K.; Tangudu, J.K.; Jahns, T.M. Comparison of Interior and Surface PM Machines Equipped with Fractional-Slot Concentrated Windings for Hybrid Traction Applications. *IEEE Trans. Energy Convers.* **2012**, *27*, 593–602. [CrossRef]
25. EL-Refaie, A.M. Fractional-Slot Concentrated-Windings Synchronous Permanent Magnet Machines: Opportunities and Challenges. *IEEE Trans. Ind. Electron.* **2010**, *57*, 107–121. [CrossRef]
26. Dogan, H.; Wurtz, F.; Foggia, A.; Garbuio, L. Analysis of Slot-Pole Combination of Fractional-Slots PMSM for Embedded Applications. In Proceedings of the International Aegean Conference on Electrical Machines and Power Electronics and Electromotion, Istanbul, Turkey, 8–10 September 2011.

27. Mamur, H.; Sahin, C.; Karacor, M.; Bhuiyan, M.R.A. Design and fabrication of an outer rotor permanent magnet synchronous generator with fractional winding for micro-wind turbines. *IET* **2020**, *14*, 2273–2282.
28. Kim, S.Y.; Cho, J.H.; Lee, S.T.; Lee, S.G. Study of Characteristics According to Pole–Slot Combination of Fractional Slot Concentrated Winding Permanent Magnet Synchronous Motor. *J. Electr. Eng. Technol.* **2024**, 2093–7423. [CrossRef]
29. Liu, Y.; Zhu, Z.Q.; Gan, C.; Brockway, S.; Hilton, C. Comparison of optimal slot/pole number combinations in fractional slot permanent magnet synchronous machines having similar slot and pole numbers. *IET* **2019**, *2019*, 4585–4589.
30. Miller, T.J.E. *Brushless Permanent-Magnet and Reluctance Motor Drives*; Oxford University Press: Oxford, UK, 1989; ISBN 0-19-859369-4.
31. Kim, D.H.; Kim, K.S.; Yang, I.J.; Lee, J.; Kim, W.H. Alternative Bridge Spoke Permanent Magnet Synchronous Generator Design for Wind Power Generation Systems. *IEEE Access* **2021**, *9*, 152819–152828. [CrossRef]
32. Park, Y.; Kim, H.; Jang, H.; Ham, S.H.; Lee, J.; Jung, D.H. Efficiency Improvement of Permanent Magnet BLDC With Halbach Magnet Array for Drone. *IEEE Trans. Appl. Supercond.* **2020**, *3*, 5201405. [CrossRef]
33. Lee, C.-S.; Kim, H.-J. Induced EMF THD Reduction Design of Permanent Magnet Synchronous Generators for Diesel Engine Generators. *Processes* **2021**, *9*, 986. [CrossRef]
34. Bianchi, N.; Fornasiero, E. Impact of MMF Space Harmonic on Rotor Losses in Fractional-Slot Permanent-Magnet Machines. *IEEE Trans. Energy Convers.* **2009**, *24*, 323–328. [CrossRef]
35. Bianchi, N. Permanent magnet synchronous motors. In *Industrial Electronics Handbooks*, 2nd ed.; Power Electronics and Motor Drives; CRC Press: Boca Raton, FL, USA, 2011.
36. Refaie, A.M.; Jahns, T.M. Optimal flux weakening in surface PM machines using fractional-slot concentrated windings. *IEEE Trans. Ind. Appl.* **2005**, *41*, 790–800. [CrossRef]
37. Zhu, L.; Zhu, Z.Q.; Chan, C.C. Analytical Methods for Minimizing Cogging Torque in Permanent-Magnet Machines. *IEEE Trans. Magn.* **2009**, *45*, 2023–2031. [CrossRef]
38. Ouamara, D.; Dubas, F. Permanent-Magnet Eddy-Current Losses: A Global Revision of Calculation and Analysis. *Math. Comput. Appl.* **2019**, *24*, 67. [CrossRef]

Disclaimer/Publisher's Note: The statements, opinions and data contained in all publications are solely those of the individual author(s) and contributor(s) and not of MDPI and/or the editor(s). MDPI and/or the editor(s) disclaim responsibility for any injury to people or property resulting from any ideas, methods, instructions or products referred to in the content.